



# Unprecedented effect of CO<sub>2</sub> calcination atmosphere on photocatalytic H<sub>2</sub> production activity from water using g-C<sub>3</sub>N<sub>4</sub> synthesized from triazole polymerization

Jing Xu<sup>a,b</sup>, Mamoru Fujitsuka<sup>a</sup>, Sooyeon Kim<sup>a</sup>, Zhouping Wang<sup>b</sup>, Tetsuro Majima<sup>a,\*</sup>

<sup>a</sup> The Institute of Scientific and Industrial Research (SANKEN), Osaka University, Mihogaoka 8-1, Ibaraki, Osaka 567-0047, Japan

<sup>b</sup> School of Food Science and Technology, Jiangnan University, Lihu Avenue 1800, Wuxi 214122, PR China

## ARTICLE INFO

### Keywords:

Photocatalysis  
g-C<sub>3</sub>N<sub>4</sub>  
CO<sub>2</sub> atmosphere  
Hydrogen  
Evolution reaction  
Triazole

## ABSTRACT

Gaseous atmosphere during graphitic carbon nitride (g-C<sub>3</sub>N<sub>4</sub>) preparation can have a significant influence on modifying the morphological texture, polymeric structure, charge carrier behavior, and consequently the photocatalytic performance. Herein, we developed a new one-step method to fabricate g-C<sub>3</sub>N<sub>4</sub> through direct pyrolysis of 3-amino-1,2,4-triazole in CO<sub>2</sub> atmosphere (C<sub>3</sub>N<sub>4</sub>-T-CO<sub>2</sub>) with no additive. Surprisingly, the H<sub>2</sub> production activity of C<sub>3</sub>N<sub>4</sub>-T-CO<sub>2</sub> photocatalyst under visible light irradiation was 2.4 and 1.7 times as high as that of g-C<sub>3</sub>N<sub>4</sub> obtained under air and N<sub>2</sub> atmosphere with the same heating process, respectively. Detailed characterizations indicated that the CO<sub>2</sub> calcination atmosphere induced less nitrogen vacancies with no charge transport ability, more NH<sub>x</sub> groups, and faster rate of the electron transport between heptazine rings for C<sub>3</sub>N<sub>4</sub>-T-CO<sub>2</sub> among three samples. It is also suggested that the larger number of NH<sub>x</sub> in C<sub>3</sub>N<sub>4</sub>-T-CO<sub>2</sub> could enhance the interlayer electron transport through the hydrogen-bonding interaction between C<sub>3</sub>N<sub>4</sub> layers. Time-resolved photoluminescence, single-particle fluorescence, and femtosecond time-resolved transient absorption measurements were performed to elucidate the efficient charge transfer and trapping processes in C<sub>3</sub>N<sub>4</sub>-T-CO<sub>2</sub>. For the first time, such unprecedented effect of CO<sub>2</sub> calcination atmosphere was observed for g-C<sub>3</sub>N<sub>4</sub>. This work not only presents a promising strategy in designing highly effective g-C<sub>3</sub>N<sub>4</sub> photocatalyst for solar energy conversion, but also makes an insight into the charge transfer process in g-C<sub>3</sub>N<sub>4</sub> photocatalyst.

## 1. Introduction

Photocatalytic hydrogen (H<sub>2</sub>) production from water is regarded as one promising strategy to solve the global energy crisis by utilizing solar energy. Therefore, developing effective and stable photocatalysts for hydrogen evolution reaction (HER) has become one of the most significant and challenging research subjects in the recent decades. Among the numerous kinds of existing semiconductors, graphitic carbon nitride (g-C<sub>3</sub>N<sub>4</sub>) has drawn considerable attention since the pioneering work on its HER ability published in 2009 by Wang et al. [1]. g-C<sub>3</sub>N<sub>4</sub>, which is constructed from N-bridged triazine or tri-s-triazine (heptazine) repeating units, can be synthesized by thermal condensation of diverse nitrogen-rich precursors, for instance, cyanamide, dicyandiamide, melamine, thiourea and so on [2]. As an organic polymeric photocatalyst, g-C<sub>3</sub>N<sub>4</sub> shows extensive potential in energetic and environmental applications including water splitting [3,4], pollutants degradation [5,6], CO<sub>2</sub> reduction [7,8], disinfection [9,10], and

N<sub>2</sub> fixation [11,12] in virtue of its low cost, environment-friendly nature, visible-light response, and appropriate band structure. However, the efficiencies of bulk g-C<sub>3</sub>N<sub>4</sub> in the above applications are not sufficiently high, because of the limited visible-light adsorption, low specific surface area, less active sites, fast charge recombination, and slow charge separation [13]. As the flexible supramolecular framework of g-C<sub>3</sub>N<sub>4</sub> allows the feasibility of tuning its textural and chemical structures for photocatalysis, various approaches have been applied to overcome the existing obstacles and enhance the photocatalytic activity of g-C<sub>3</sub>N<sub>4</sub>, such as morphology control [14,15], heteroatoms doping [16,17], heterostructures constructing [18,19], and copolymerization with proper monomers [20,21]. Nonetheless, most of the above methods require complicated synthesis procedures and costly functionalized reagents which are unsuitable for practical application. Thus, it is still desirable to develop an alternative simple and inexpensive method to modify characteristic structure and improve photocatalytic performance of g-C<sub>3</sub>N<sub>4</sub>.

\* Corresponding author.

E-mail address: [majima@sanken.osaka-u.ac.jp](mailto:majima@sanken.osaka-u.ac.jp) (T. Majima).

<https://doi.org/10.1016/j.apcatb.2018.09.023>

Received 10 July 2018; Received in revised form 4 September 2018; Accepted 8 September 2018

Available online 09 September 2018

0926-3373/ © 2018 Elsevier B.V. All rights reserved.

It is well known that optical, morphological, electronic, and photocatalytic properties of g-C<sub>3</sub>N<sub>4</sub> can be greatly affected by the pyrolysis conditions set in g-C<sub>3</sub>N<sub>4</sub> preparation process, including the precursors, temperature-rise path, thermolysis temperature, and heating duration [22,23]. Additionally, the calcination atmospheres, such as H<sub>2</sub> and NH<sub>3</sub>, can also exert an effect on the intrinsic structure and charge carrier behavior of g-C<sub>3</sub>N<sub>4</sub> via generating defects, carbon or nitrogen vacancies, and disordered conjugated planes, and consequently improve the photocatalytic activity [24–28]. For example, H<sub>2</sub> causes g-C<sub>3</sub>N<sub>4</sub> with more nitrogen vacancies during thermal condensation of dicyandiamide [29], while NH<sub>3</sub> does holey g-C<sub>3</sub>N<sub>4</sub> nanosheets with carbon vacancies by heating bulk g-C<sub>3</sub>N<sub>4</sub> [30]. Pyrolysis-generated self-producing atmosphere results in porous g-C<sub>3</sub>N<sub>4</sub> with more uncondensed amino groups by heating melamine [31]. The previous works not only present an insight into the influence of the reaction atmosphere on the structure and properties of g-C<sub>3</sub>N<sub>4</sub>, but also arise our interest to develop a facile method to synthesize active g-C<sub>3</sub>N<sub>4</sub> under appropriate atmosphere.

Recently, substituted 1,2,4-triazoles, heterocyclic nitrogen-rich molecules with a five-membered ring of three nitrogen and two carbon atoms, were found to be one kind of outstanding precursors for the synthesis of g-C<sub>3</sub>N<sub>4</sub> with heptazine-based polymeric melon structure [32,33]. In the previous studies, triazole-derived g-C<sub>3</sub>N<sub>4</sub> possessed expanded visible light absorption, adjusted electronic structures, and altered emission properties which resulted in significantly enhanced photocatalytic activities compared to ordinary g-C<sub>3</sub>N<sub>4</sub> with a band gap of ~2.7 eV [34,35]. Herein, we fabricated g-C<sub>3</sub>N<sub>4</sub> through directly pyrolysis treatment of 3-amino-1,2,4-triazole in CO<sub>2</sub> atmosphere (C<sub>3</sub>N<sub>4</sub>-T-CO<sub>2</sub>) with no additive. For comparison, g-C<sub>3</sub>N<sub>4</sub> was prepared under air and N<sub>2</sub> calcination atmosphere with the same heating process. Impressively, the obtained C<sub>3</sub>N<sub>4</sub>-T-CO<sub>2</sub> photocatalyst showed higher H<sub>2</sub> production activity under visible light irradiation than g-C<sub>3</sub>N<sub>4</sub> synthesized in air and N<sub>2</sub>. Moreover, the impact of CO<sub>2</sub> atmosphere on the formation of the heptazine-based polymeric melon structure and the charge transfer process was also systematically studied to understand the higher activity of C<sub>3</sub>N<sub>4</sub>-T-CO<sub>2</sub>. To the best of our knowledge, this is the first time that such unprecedented effect of CO<sub>2</sub> calcination atmosphere was observed for g-C<sub>3</sub>N<sub>4</sub> photocatalyst. Considering the simple synthesis and high activity of C<sub>3</sub>N<sub>4</sub>-T-CO<sub>2</sub>, this work clearly presents a method in designing the highly effective g-C<sub>3</sub>N<sub>4</sub> photocatalyst.

## 2. Experimental section

### 2.1. Preparation of C<sub>3</sub>N<sub>4</sub>-T under different atmospheres

We prepared a variety of g-C<sub>3</sub>N<sub>4</sub> via thermal polycondensation of various precursors (X), C<sub>3</sub>N<sub>4</sub>-X (X = melamine (M), 3-amino-1,2,4-triazole (T), dicyandiamide (D), and thiourea (TU)). The photocatalytic H<sub>2</sub> production activities of C<sub>3</sub>N<sub>4</sub>-X photocatalyst were examined under the experimental conditions denoted in the next paragraph. Among C<sub>3</sub>N<sub>4</sub>-X photocatalysts, C<sub>3</sub>N<sub>4</sub>-T photocatalyst shows the highest activity for H<sub>2</sub> production from water under visible light irradiation ( $\lambda \geq 420$  nm) (Fig. S1). Similarly, the high photocatalytic activity of C<sub>3</sub>N<sub>4</sub>-T photocatalyst has been previously reported by other groups [2,34].

Since C<sub>3</sub>N<sub>4</sub>-T photocatalyst has the highest activity, we studied the synthesis of C<sub>3</sub>N<sub>4</sub>-T under three kinds of calcination atmospheres (Y = N<sub>2</sub>, air, and CO<sub>2</sub>). Three C<sub>3</sub>N<sub>4</sub>-T-Y were prepared by calcinating T (0.2 g) at 550 °C for 4 h after heating from room temperature up to 550 °C at a rate of 3 °C min<sup>-1</sup> under N<sub>2</sub>, air, or CO<sub>2</sub>, which are denoted by C<sub>3</sub>N<sub>4</sub>-T-N<sub>2</sub>, C<sub>3</sub>N<sub>4</sub>-T-air, and C<sub>3</sub>N<sub>4</sub>-T-CO<sub>2</sub>, respectively. The bulk g-C<sub>3</sub>N<sub>4</sub> synthesized from M (C<sub>3</sub>N<sub>4</sub>-M), C<sub>3</sub>N<sub>4</sub>-T-N<sub>2</sub>, and C<sub>3</sub>N<sub>4</sub>-T-air were all selected as the reference g-C<sub>3</sub>N<sub>4</sub> samples.

### 2.2. Photocatalytic H<sub>2</sub> production

The photocatalytic H<sub>2</sub> production activities were evaluated under

visible light irradiation by a xenon lamp together with a 420 nm cutoff filter (Asahi Spectra HAL-320, 750 mW cm<sup>-2</sup>). 5 mg of as-prepared photocatalyst was ultrasonically dispersed in 5 mL aqueous solution containing 20 vol% triethanolamine (TEOA) as a sacrificial electron donor. Then 3 wt% Pt was deposited on the surface of photocatalyst as a cocatalyst from photoreduction of H<sub>2</sub>PtCl<sub>6</sub>. The suspension of photocatalyst was purged with Ar for 30 min to remove air completely in the reactor and sealed with a rubber plug. After the photocatalytic reactions, the volume of evolved H<sub>2</sub> was measured by a Shimadzu GC-8A gas chromatograph equipped with a thermal conductive detector and a MS-5A column, using Ar carrier gas. The stability of C<sub>3</sub>N<sub>4</sub>-T-CO<sub>2</sub> photocatalyst was examined by reusing them in cycle experiments. The apparent quantum efficiency (AQE) for hydrogen production at different wavelengths of monochromatic light was calculated from Eq. (1) [18],

$$AQE = \frac{2 \times \text{number of produced } H_2}{\text{number of absorbed photons}} \times 100 (\%). \quad (1)$$

### 2.3. Characterization

X-ray diffraction (XRD) patterns were collected in a Rigaku Rint-2500 Smartlab system with a Cu K $\alpha$  radiation. Fourier transformed infrared (FTIR) measurements were conducted by a PerkinElmer spectrometer. The morphological images of samples were taken using scanning electron microscopy (SEM, JEOL JSM-6330FT) and transmission electron microscopy (TEM, JEOL-2100). The Brunauer-Emmett-Teller (BET) surface area and pore size distribution were estimated by N<sub>2</sub> sorption with a BELSORP max (BEL Japan). UV-vis diffuse reflectance spectra (DRS) were recorded on a Jasco V-770 spectrometer. Elemental analysis was carried out by a MICRO CORDER JM10. X-ray photoelectron spectroscopy (XPS) analysis was characterized by an AXIS-165x system (Shimadzu), and C 1s at 284.8 eV was used to internally calibrate the binding energies. Steady-state photoluminescence (PL) spectra were obtained on a Horiba FluoroMax-4 fluorescence spectrometer excited at 350 nm. Time-resolved fluorescence spectra were measured by the single photon counting method in a streakscope (Hamamatsu Photonics, C4334-01) equipped with a polychromator (Acton Research, SpectraPro150), and a 400-nm femtosecond pulse laser was used as the excitation source. The fluorescence and background signals were both detected respectively by photomultiplier. The fluorescence lifetimes of the samples were estimated from deconvolution of the fluorescence and background signals.

The details of the characterizations such as photoelectrochemical measurements, single particle fluorescence analysis, and femtosecond time-resolved diffuse reflectance (fs-TDR) spectroscopy were summarized in Supporting Information.

## 3. Results and discussion

### 3.1. Characterization of C<sub>3</sub>N<sub>4</sub>-T-Y

The crystal and chemical structures of as-prepared C<sub>3</sub>N<sub>4</sub>-T-Y were characterized by XRD and FTIR spectra, respectively. The XRD patterns show two characteristic peaks at 13.1° and 27.6° assigned to in-planar packing of heptazine units and inter-planar stacking of conjugated C–N heterocycles, respectively (Fig. S2) [1], suggesting the heptazine ring-based framework of C<sub>3</sub>N<sub>4</sub>-T-Y. The FTIR spectra of C<sub>3</sub>N<sub>4</sub>-T-Y display three characteristic absorption bands of g-C<sub>3</sub>N<sub>4</sub> at 808, 1200–1700, and 3150 cm<sup>-1</sup>, assigned to the breathing vibration of the heptazine units, the stretching vibration of aromatic heterocycles, and the stretching vibration of N–H bonds, respectively (Fig. S3) [1]. Since no obvious difference is observed for three C<sub>3</sub>N<sub>4</sub>-T-Y, they have similar crystal and chemical structures.

The morphological characteristics of C<sub>3</sub>N<sub>4</sub>-T-Y were studied by SEM and TEM. The SEM images exhibit micrometer-sized stacking particles

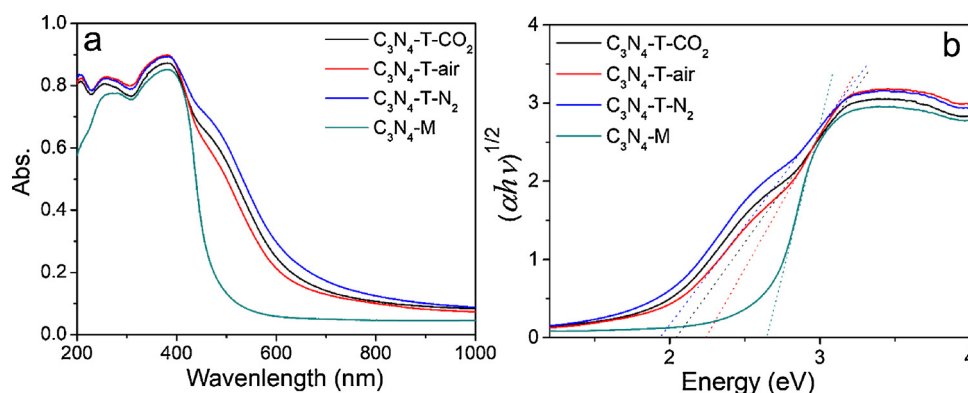


Fig. 1. UV-vis diffuse reflectance spectra (a) and band gap energy calculation (b) of  $C_3N_4$ -T-Y and  $C_3N_4$ -M.

together with irregular shapes (Fig. S4), while the TEM images do bulk morphology with lamellar structure (Fig. S5). Three  $C_3N_4$ -T-Y show similar BET surface area ( $6.2\text{--}7.2\text{ m}^2\text{ g}^{-1}$ ), pore volume ( $0.060\text{--}0.072\text{ cm}^3\text{ g}^{-1}$ ), and pore size distribution (Table S1 and Fig. S6), confirming the similar morphology.

By changing Y of  $C_3N_4$ -T-Y from air to  $CO_2$  and  $N_2$ , the color of  $C_3N_4$ -T-Y gradually darkens and finally turns brick-red (Fig. S7), which are reflected to the absorption property analyzed by DRS spectra (Fig. 1a). Three  $C_3N_4$ -T-Y exhibit two absorption bands at 400 and 450–800 nm. The absorption band at 400 nm is observed for  $C_3N_4$ -M, while  $C_3N_4$ -M has no shoulder peak at 450–800 nm. Among three  $C_3N_4$ -T-Y,  $C_3N_4$ -T- $N_2$  has stronger absorption at 450–800 nm, while  $C_3N_4$ -T-air does weaker absorption. One intrinsic band at 400 nm is attributed to  $\pi\text{--}\pi^*$  transition in the conjugated heptazine ring, while other band at 450–800 nm originates from  $n\text{--}\pi^*$  transition involving lone pair electrons of  $sp^3$  N atoms of  $NH_x$  substituted on heptazine ring [36]. The  $n\text{--}\pi^*$  transition is allowed for dissymmetric heptazine units which can be induced by nitrogen vacancies ( $V_N$ ) [37]. Since  $V_N$  increases in the order of  $C_3N_4$ -T-air <  $C_3N_4$ -T- $CO_2$  <  $C_3N_4$ -T- $N_2$ , the ring should be deformed more considerably in the same order. The relation between  $V_N$  and photocatalytic activity changes has been reported for other  $g\text{-}C_3N_4$  containing  $V_N$  [38,39].

The band gaps of  $C_3N_4$ -T-air,  $C_3N_4$ -T- $CO_2$ , and  $C_3N_4$ -T- $N_2$  are calculated from Tauc-Plot (Fig. 1b) to be 2.24, 2.05, and 1.94 eV, respectively, which are significantly smaller than 2.65 eV of  $C_3N_4$ -M. The band-gap decrease or absorption increase in the visible range is responsible for higher activity of  $C_3N_4$ -T photocatalyst than  $C_3N_4$ -M photocatalyst for  $H_2$  production from water under visible light irradiation (Fig. S1) [2]. It is clear that the band gap is influenced by the calcination atmospheres. Alternatively,  $C_3N_4$ -T has defect sites depending on the calcination atmospheres.

The existence of  $V_N$  in heptazine ring of  $C_3N_4$ -T-Y was validated by elemental analysis. The C/N atomic ratio is 0.657 for  $C_3N_4$ -T-air, and gradually increases to 0.660 and 0.665 for  $C_3N_4$ -T- $CO_2$  and  $C_3N_4$ -T- $N_2$ , respectively (Table S2). The elemental analysis suggests the increasing loss of N atom and the increasing number of  $V_N$  in the order of  $C_3N_4$ -T-air <  $C_3N_4$ -T- $CO_2$  <  $C_3N_4$ -T- $N_2$  [40].

XPS was further conducted to confirm the formation of  $V_N$  and investigate the chemical states of  $C_3N_4$ -T-Y. The XPS C 1s spectra comprise C ( $C\text{--}N\text{=C}$ ) in heptazine rings and adventitious C, showing no obvious change for three  $C_3N_4$ -T-Y (Fig. S8). The XPS N 1s spectra display three peaks including N ( $C\text{--}N\text{=C}$ ) in heptazine rings (398.8 eV), N in  $N\text{--}(C)_3$  (400.1 eV), and N in  $NH_x$  (401.2 eV) (Fig. 2) [9]. As shown in Table 1, the ratio of peak area  $C\text{--}N\text{=C}$  vs.  $N\text{--}(C)_3$  ( $C\text{--}N\text{=C}/N\text{--}(C)_3$ ) increases in the order of  $C_3N_4$ -T- $N_2$  (3.9) <  $C_3N_4$ -T- $CO_2$  (4.4) <  $C_3N_4$ -T-air (5.1), suggesting  $V_N$  are originated by releasing N ( $C\text{--}N\text{=C}$ ) to lead the degradation of the heptazine rings in a part [7]. Additionally,  $C\text{--}N\text{=C}/N\text{--}(C)_3$  ratio of  $C_3N_4$ -T- $N_2$  (3.9) is even 0.5 lower than that of  $C_3N_4$ -T- $CO_2$  (4.4), indicating that more  $V_N$  are formed

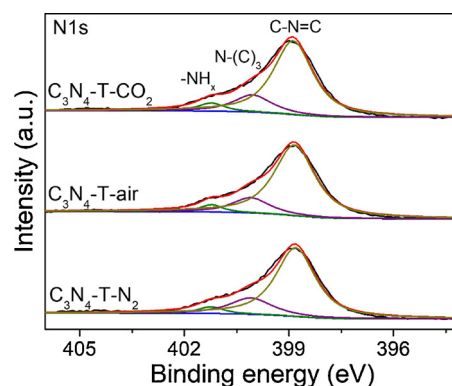


Fig. 2. XPS N 1s spectra of  $C_3N_4$ -T-Y.

Table 1

Distribution of N atoms based on XPS N 1s spectra for  $C_3N_4$ -T-Y.

$C_3N_4$ -T-Y	$C\text{--}N\text{=C}$	$N\text{--}(C)_3$	$NH_x$	$C\text{--}N\text{=C}/N\text{--}(C)_3$	$NH_x/N\text{--}(C)_3$
$C_3N_4$ -T- $N_2$	75.96%	19.28%	4.76%	3.9	0.25
$C_3N_4$ -T-air	79.84%	15.62%	4.54%	5.1	0.29
$C_3N_4$ -T- $CO_2$	76.96%	17.35%	5.69%	4.4	0.33

under  $N_2$  calcination atmosphere, which coincides with the DRS and elemental analysis. Meanwhile, the ratio of  $NH_x/N\text{--}(C)_3$  for  $C_3N_4$ -T- $CO_2$  (0.33) is larger than those for  $C_3N_4$ -T- $N_2$  (0.25) and  $C_3N_4$ -T-air (0.29). As previously reported, hydrogen-bonding interaction between  $C_3N_4$  layers can be arisen from the presence of  $NH_x$  groups [31]. Therefore,  $C_3N_4$ -T- $CO_2$  with the highest ratio of  $NH_x/N\text{--}(C)_3$  contains the largest number of  $NH_x$  groups to promote the interaction between  $C_3N_4$  layers through the hydrogen bonding, which would also be proved by the higher  $H_2$  production activity and better photoelectrochemical performance for  $C_3N_4$ -T- $CO_2$  photocatalyst than  $C_3N_4$ -T- $N_2$  and  $C_3N_4$ -T-air photocatalysts as discussed below.

### 3.2. Photocatalytic $H_2$ production activity

To explore the effects of calcination atmosphere on the activity of  $C_3N_4$ -T-Y photocatalyst,  $H_2$  production from water was carried out under visible light irradiation ( $\lambda \geq 420\text{ nm}$ ) by adding TEOA as the sacrificial electron donor and depositing Pt as the cocatalyst (Fig. 3a). The control experiment indicates that  $H_2$  is barely produced without photocatalyst or light irradiation. Although  $C_3N_4$ -T- $N_2$  possesses the best light-harvesting ability and largest amount of  $V_N$ ,  $C_3N_4$ -T- $CO_2$  exhibits the highest photocatalytic activity of  $H_2$  production ( $424.7\text{ }\mu\text{mol g}^{-1}\text{ h}^{-1}$ ), which is almost 2.4 and 1.7 times as large as  $C_3N_4$ -T- $N_2$  ( $177.2\text{ }\mu\text{mol g}^{-1}\text{ h}^{-1}$ ) and  $C_3N_4$ -T-air ( $253.1\text{ }\mu\text{mol g}^{-1}\text{ h}^{-1}$ ),

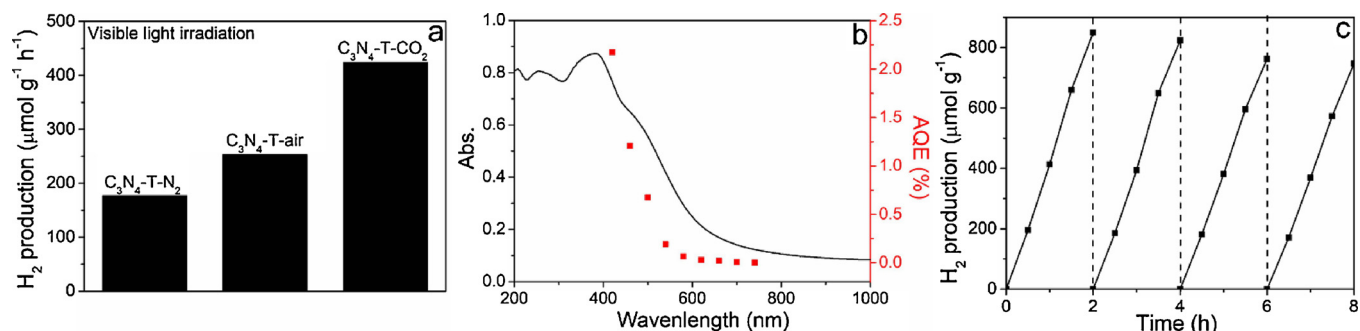


**Fig. 3.** Comparison of the H<sub>2</sub> production rate of C<sub>3</sub>N<sub>4</sub>-T-Y photocatalyst (a), absorption spectrum and wavelength-dependent AQE of H<sub>2</sub> production for C<sub>3</sub>N<sub>4</sub>-T-CO<sub>2</sub> photocatalyst (b), stability of C<sub>3</sub>N<sub>4</sub>-T-CO<sub>2</sub> photocatalyst for the photocatalytic H<sub>2</sub> production (c).

respectively. Therefore, the highest activity of C<sub>3</sub>N<sub>4</sub>-T-CO<sub>2</sub> photocatalyst arises from neither absorption spectrum nor band gap, but other factors. Surprisingly, such unprecedented effect of CO<sub>2</sub> calcination atmosphere has never been observed for C<sub>3</sub>N<sub>4</sub> in HER.

To elucidate the unprecedented effect of CO<sub>2</sub> atmosphere on the photocatalytic activity, we carried out various measurements for C<sub>3</sub>N<sub>4</sub>-T-CO<sub>2</sub> as shown below. The wavelength-dependent AQE (Fig. 3b) clearly shows that the photocatalytic activity of H<sub>2</sub> production for C<sub>3</sub>N<sub>4</sub>-T-CO<sub>2</sub> is not coincident with the DRS spectrum. Although the activity is related to the absorption in the range of UV and visible light shorter than 460 nm, it is smaller than the expected values in the range of 460–800 nm. It is, therefore, clear that the  $\pi$ - $\pi^*$  transition plays a dominant role in the overall visible-light-driven activity of C<sub>3</sub>N<sub>4</sub>-T-CO<sub>2</sub> photocatalyst, while the  $n$ - $\pi^*$  transition just makes a minor contribution to the photocatalytic activity. Additionally, the AQE of C<sub>3</sub>N<sub>4</sub>-T-CO<sub>2</sub> at 420 nm is about 2.2%, which is larger than those of C<sub>3</sub>N<sub>4</sub>-T-N<sub>2</sub> (1.1%) and C<sub>3</sub>N<sub>4</sub>-T-air (1.3%). In contrast, it has been reported that the generated V<sub>N</sub> in g-C<sub>3</sub>N<sub>4</sub> leads to improved photocatalytic activity because of obvious red-shift of the intrinsic and shoulder absorption peaks [29,39]. The difference is discussed below.

The stability of C<sub>3</sub>N<sub>4</sub>-T-CO<sub>2</sub> photocatalyst was also examined to show a negligible decrease of the H<sub>2</sub> production rate after 4 cycles (Fig. 3c), confirming that C<sub>3</sub>N<sub>4</sub>-T-CO<sub>2</sub> acts as a stable photocatalyst for H<sub>2</sub> evolution.

### 3.3. Photophysical and photochemical properties

To clarify the roles of V<sub>N</sub> and NH<sub>x</sub> for the activity of C<sub>3</sub>N<sub>4</sub>-T-CO<sub>2</sub> photocatalyst, photoelectrochemical experiments, steady state PL, time-resolved fluorescence, single particle fluorescence, and fs-TDR measurements were performed to investigate the charge transfer process of C<sub>3</sub>N<sub>4</sub>-T-Y in detail.

Three C<sub>3</sub>N<sub>4</sub>-T-Y electrodes can generate quick and invertible

transient photocurrent responses by the intermittent irradiation (Fig. 4a). Among them, the C<sub>3</sub>N<sub>4</sub>-T-CO<sub>2</sub> electrode exhibits the largest visible-light-driven current density which is consistent with the highest H<sub>2</sub> production rate for C<sub>3</sub>N<sub>4</sub>-T-CO<sub>2</sub>. The enhanced transient photocurrent response can be explained by the higher separation efficiency of electron-hole pairs for C<sub>3</sub>N<sub>4</sub>-T-CO<sub>2</sub> [9]. The consistent result was observed in electrochemical impedance spectroscopy (EIS) Nyquist plots (Fig. 4b), in which arc radius of C<sub>3</sub>N<sub>4</sub>-T-CO<sub>2</sub> is smaller than those of C<sub>3</sub>N<sub>4</sub>-T-N<sub>2</sub> and C<sub>3</sub>N<sub>4</sub>-T-air under visible light irradiation. Since a smaller EIS arc radius is indicative of a lower charge transfer resistance of the working electrode, C<sub>3</sub>N<sub>4</sub>-T-CO<sub>2</sub> possesses more efficient charge transfer property [9].

It is found that the photocurrent and EIS performance improve in the order of C<sub>3</sub>N<sub>4</sub>-T-N<sub>2</sub> < C<sub>3</sub>N<sub>4</sub>-T-air < C<sub>3</sub>N<sub>4</sub>-T-CO<sub>2</sub>, and they are not directly influenced by V<sub>N</sub> and degradation of heptazine rings which increase in the order of C<sub>3</sub>N<sub>4</sub>-T-air < C<sub>3</sub>N<sub>4</sub>-T-CO<sub>2</sub> < C<sub>3</sub>N<sub>4</sub>-T-N<sub>2</sub>. On the other hand, the rising order of number of NH<sub>x</sub> (C<sub>3</sub>N<sub>4</sub>-T-N<sub>2</sub> < C<sub>3</sub>N<sub>4</sub>-T-air < C<sub>3</sub>N<sub>4</sub>-T-CO<sub>2</sub>) is similar to the order of the photocurrent and EIS. It is, therefore, suggested that the interlayer electron transport between C<sub>3</sub>N<sub>4</sub> layers is considerably enhanced in C<sub>3</sub>N<sub>4</sub>-T-CO<sub>2</sub> with larger number of NH<sub>x</sub> than those in C<sub>3</sub>N<sub>4</sub>-T-air and C<sub>3</sub>N<sub>4</sub>-T-N<sub>2</sub>. In other word, CO<sub>2</sub> calcination atmosphere provides a large interface between C<sub>3</sub>N<sub>4</sub> layers due to larger number of NH<sub>x</sub> in C<sub>3</sub>N<sub>4</sub>-T-CO<sub>2</sub> than in C<sub>3</sub>N<sub>4</sub>-T-air and C<sub>3</sub>N<sub>4</sub>-T-N<sub>2</sub>. The interfacial interaction between C<sub>3</sub>N<sub>4</sub> layers can be considerably enhanced by the hydrogen bonding between NH<sub>x</sub> groups [31].

It is well known that g-C<sub>3</sub>N<sub>4</sub> shows PL originated from the charge recombination between hole and electron under light irradiation [19]. Indeed, C<sub>3</sub>N<sub>4</sub>-M shows intense PL under 350-nm excitation, while three C<sub>3</sub>N<sub>4</sub>-T-Y do a negligible weak PL at around 480 nm (Fig. S9). The decrease of the PL intensity corresponds to charge trapping at trap sites [39]. Fig. 5a presents the PL spectra of three C<sub>3</sub>N<sub>4</sub>-T-Y in which C<sub>3</sub>N<sub>4</sub>-T-CO<sub>2</sub> and C<sub>3</sub>N<sub>4</sub>-T-air exhibit higher PL intensity than C<sub>3</sub>N<sub>4</sub>-T-N<sub>2</sub>. The

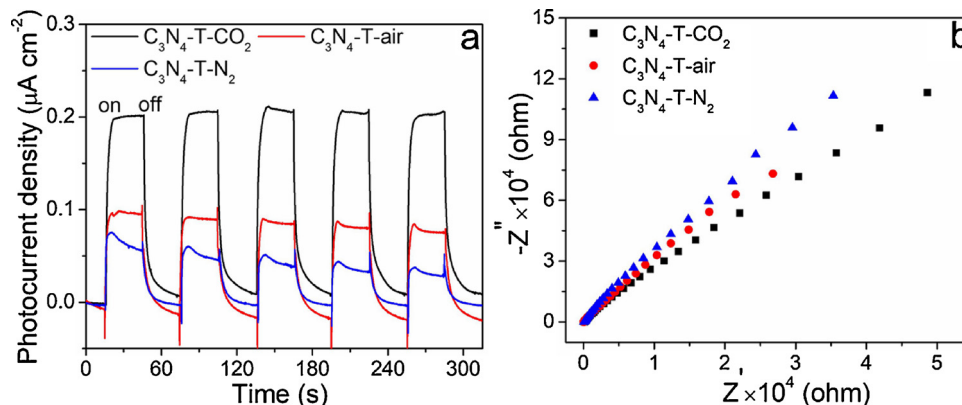


**Fig. 4.** Photocurrent responses (a) and EIS Nyquist plots (b) of C<sub>3</sub>N<sub>4</sub>-T-Y under visible light irradiation.



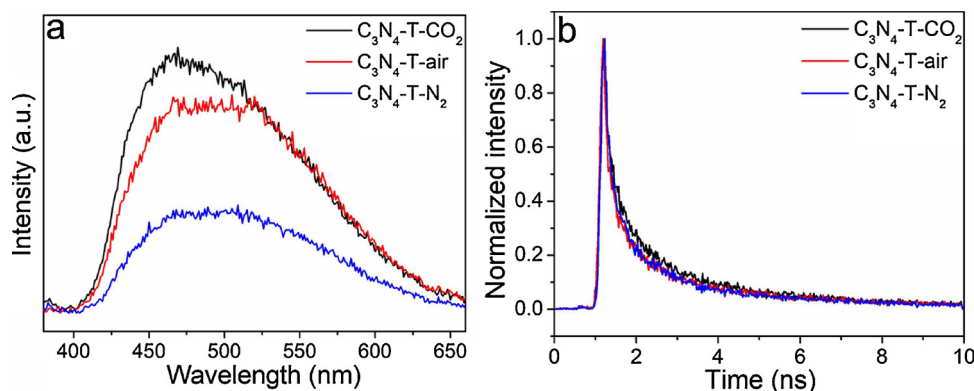


Fig. 5. PL spectra of  $C_3N_4$ -T-Y with excitation at 350 nm (a), time profiles of fluorescence decay in the ns time scale for  $C_3N_4$ -T-Y with excitation at 400 nm (b).

difference may relate to  $V_N$  as the charge trap states, while the number of  $V_N$  has no relation to the photocatalytic activity.

To understand the steady state PL results of  $C_3N_4$ -T-Y, time-resolved fluorescence spectra were measured under 400-nm laser excitation (Fig. 5b). The averaged fluorescence lifetime ( $\tau_{av}$ ) of  $\sim 1$  ns for  $C_3N_4$ -T-Y is shorter than  $\tau_{av}$  of a few ns for  $C_3N_4$ -M [9]. Usually longer  $\tau$  corresponds to higher photocatalytic activity [41]. This discrepancy can be explained by the existence of various charge trap sites with shallow and deep potential minima [42]. Notably, among three  $C_3N_4$ -T-Y,  $C_3N_4$ -T-CO<sub>2</sub> exhibits slower decay kinetics than  $C_3N_4$ -T-air and  $C_3N_4$ -T-N<sub>2</sub>. The decay profiles are well-fitted with shorter and longer lifetimes ( $\tau_1$  and  $\tau_2$ , respectively) for three  $C_3N_4$ -T-Y. As summarized in Table 2,  $\tau_1$  of 0.54 ns for  $C_3N_4$ -T-CO<sub>2</sub> decreases to 0.38 and 0.39 ns for  $C_3N_4$ -T-N<sub>2</sub> and  $C_3N_4$ -T-air, respectively, while  $\tau_2$  of 3.2 and 3.4 ns for  $C_3N_4$ -T-N<sub>2</sub> and  $C_3N_4$ -T-air, respectively, increases to 3.6 ns for  $C_3N_4$ -T-CO<sub>2</sub>, and the  $\tau_2$  components increase synchronously. In addition,  $\tau_{av}$  increases in the order of  $C_3N_4$ -T-N<sub>2</sub> (0.96 ns) <  $C_3N_4$ -T-air (1.1 ns) <  $C_3N_4$ -T-CO<sub>2</sub> (1.3 ns). Even such slightly different  $\tau_{av}$  may have a relation to the large difference of the photocatalytic activity of three  $C_3N_4$ -T-Y.

Generally, ensemble measurements such as the PL measurement give only average values of various properties to obscure the minor portion of values. Since the differences of the PL intensities and fluorescence lifetimes are resulted from the ensemble average, sometimes they may not be consistent with the photocatalytic activity. It is well known that single-particle fluorescence spectroscopy is significantly useful to observe the actual properties for each catalyst particles [19]. Thus, we carried out single-particle confocal fluorescence spectroscopic measurement to monitor the PL properties of individual micrometer-sized particles. The typical PL images and PL spectra of three individual  $C_3N_4$ -T-Y are shown in Fig. S10. Under 405-nm laser pulse excitation, we observed bright points which come from the emission of  $C_3N_4$ -T-Y. We randomly selected six points from each PL image and measured the corresponding PL intensities. The different PL intensities for various particles of  $C_3N_4$ -T-Y are due to the nonuniform thickness of  $C_3N_4$ -T sheet. Three  $C_3N_4$ -T-Y display a broad emission peak at  $\sim 480$  nm, and the PL intensities increase in the order of  $C_3N_4$ -T-N<sub>2</sub> <  $C_3N_4$ -T-air <  $C_3N_4$ -T-CO<sub>2</sub>. Time-resolved fluorescence spectra of more than thirty individual particles of  $C_3N_4$ -T-Y were measured, and the decay profiles were fitted by biexponential functions with  $\tau_1$  and  $\tau_2$ .  $\tau_1$ ,  $\tau_2$ , and  $\tau_{av}$  are  $\sim 0.8$ ,  $\sim 4.9$ , and 1.4–1.5 ns for  $C_3N_4$ -T-CO<sub>2</sub>, while  $\sim 0.6$ , 3.3–4.1, and 0.9–1.1 ns for  $C_3N_4$ -T-air,  $\sim 0.6$ , 3.3–3.8, and  $\sim 1.0$  ns for  $C_3N_4$ -T-N<sub>2</sub>,

respectively (Fig. 6). It is clearly found that the individual particles of  $C_3N_4$ -T-CO<sub>2</sub> possess longer  $\tau_1$ ,  $\tau_2$ , and  $\tau_{av}$  than  $C_3N_4$ -T-air and  $C_3N_4$ -T-N<sub>2</sub>. Particularly, a large difference of  $\tau_2$  (and  $\tau_{av}$ ) is consistent with that of the photocatalytic activity (Fig. 3).

Fs-TDR spectra were measured to elucidate the charge transfer kinetics of  $C_3N_4$ -T-Y. Under the 420-nm laser excitation, three  $C_3N_4$ -T-Y show a broad transient absorption band in the wavelength range of 850–1150 nm to be assigned to free and shallowly trapped photo-generated electrons (Fig. 7a–c). Transient absorption was observed immediately after a laser flash and then decayed up to 1010 ps. The time profiles of the transient absorption were recorded at 950 nm (Fig. 7d). The decay profiles were fitted by biexponential functions with shorter and longer lifetimes,  $\tau_{abs1}$  and  $\tau_{abs2}$ , respectively, which are much shorter than of PL  $\tau_1$  and  $\tau_2$ , respectively. It is, therefore, suggested that there are two kinds of charge trap sites, shallow and deep trap sites [42]. The charge recombination of shallowly trapped photo-generated electrons proceeds in the time scales of  $\tau_{abs1}$  and  $\tau_{abs2}$  with shorter and longer distances, respectively, while the charge recombination of deeply trapped photogenerated electrons occurs in the time scales of  $\tau_1$  and  $\tau_2$ . The shallow trap sites are probably assigned to the defect states, while the deep trap sites are  $V_N$  as discussed above.  $\tau_{abs1}$  and  $\tau_{abs2}$  are 38 and 1069 ps for  $C_3N_4$ -T-CO<sub>2</sub>, respectively, while they are 36 and 853 ps for  $C_3N_4$ -T-N<sub>2</sub>, 31 and 957 ps for  $C_3N_4$ -T-air (Table 3). The average lifetime ( $\tau_{abs,av}$ ) is 605 ps for  $C_3N_4$ -T-CO<sub>2</sub>, longer than 436 ps for  $C_3N_4$ -T-N<sub>2</sub> and 503 ps for  $C_3N_4$ -T-air, which can be explained by the faster electron transfer between heptazine rings in  $C_3N_4$ -T-CO<sub>2</sub> than in  $C_3N_4$ -T-N<sub>2</sub> and  $C_3N_4$ -T-air. The longer  $\tau_{abs}$  in  $C_3N_4$ -T-CO<sub>2</sub> corresponds to increasing electrons at the active sites, resulting in the enhanced photocatalytic activity [43].

### 3.4. Photocatalytic reaction mechanism

Based on the experimental results, we suggest the photocatalytic H<sub>2</sub> production mechanism for  $C_3N_4$ -T-Y photocatalyst involving band-gap excitation, charge separation to generate holes and electrons, holes removal by TEOA, electrons trapping at shallow and deep trap states (defects and  $V_N$ , respectively), charge recombination for shorter and longer distances,  $V_N$  as the electron trap sites with no charge transport ability, electron transport processes between heptazine rings in intralayer and interlayers of  $C_3N_4$ -T-Y up to Pt nanoparticles, and proton reduction on the Pt nanoparticles (Scheme 1). Firstly, band-gap excitation generates the electron-hole pairs. The holes are removed by TEOA, while electrons are accumulated in the CB band and partly trapped by shallow and deep trap states. The charge recombination of shallow and deep trap sites proceeds at shorter and longer distances.

Among three  $C_3N_4$ -T-Y photocatalysts,  $C_3N_4$ -T-CO<sub>2</sub> exhibits the highest photocatalytic H<sub>2</sub> production activity. Such unprecedented effect of CO<sub>2</sub> calcination atmosphere was firstly observed for  $C_3N_4$ -T-Y, while it has never been reported for other  $C_3N_4$ -X. The CO<sub>2</sub> calcination

Table 2

Fluorescence lifetimes ( $\tau$ ) for  $C_3N_4$ -T-Y.

$C_3N_4$ -T-Y	$\tau_1$ (ns)	$A_1$	$\tau_2$ (ns)	$A_2$	$\tau_{av}$ (ns)
$C_3N_4$ -T-N <sub>2</sub>	0.38	0.794	3.2	0.206	0.96
$C_3N_4$ -T-air	0.39	0.774	3.4	0.226	1.1
$C_3N_4$ -T-CO <sub>2</sub>	0.54	0.743	3.6	0.257	1.3

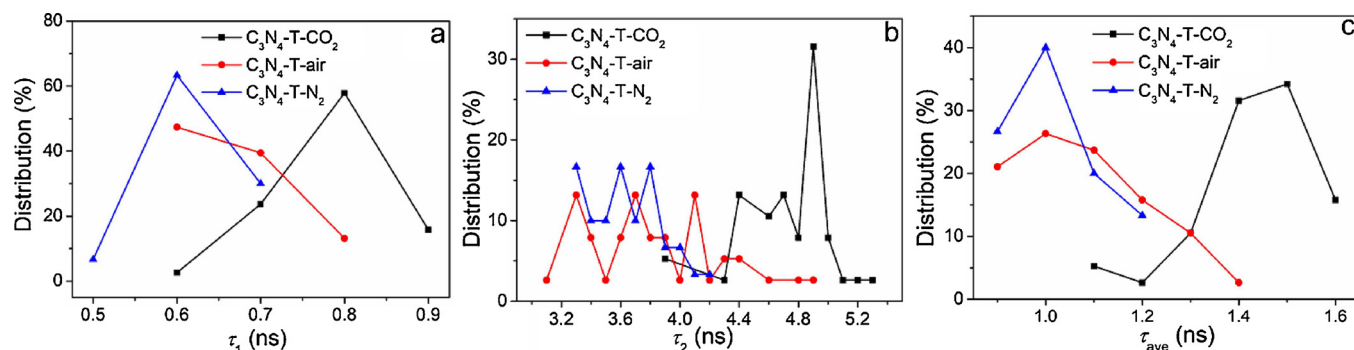


Fig. 6. Distribution of  $\tau_1$  (a),  $\tau_2$  (b), and  $\tau_{av}$  (c) for  $C_3N_4$ -T-Y obtained from single-particle confocal fluorescence spectroscopic measurements.

atmosphere induces less  $V_N$ , more  $NH_x$ , and faster rate of the electron transport between heptazine rings for  $C_3N_4$ -T- $CO_2$  among three  $C_3N_4$ -T-Y. Heptazine rings and  $NH_x$  sites are formed during the polymerization of  $C_3N_4$  precursors X, while degradation of heptazine rings competitively occurs to generate  $V_N$ . The formation of heptazine rings and  $NH_x$  sites could be enhanced during synthesis of  $C_3N_4$ -T- $CO_2$ , while the degradation of heptazine rings to generate  $V_N$  is inhibited under  $CO_2$  calcination atmosphere. It is also suggested that the interlayer electron transport between  $C_3N_4$  layers is considerably enhanced in  $C_3N_4$ -T- $CO_2$  compared with those in  $C_3N_4$ -T-air and  $C_3N_4$ -T- $N_2$ . These are probably resulted from  $CO_2$  property for the interaction with the surface of  $C_3N_4$  during T calcination process. On the other hand, no such effect could be existed for  $O_2$  and  $N_2$  calcination atmosphere. One of the different characters between  $CO_2$  and diatomic molecules,  $O_2$  and  $N_2$ , is ionic  $CO_2$  and non-ionic  $O_2$  and  $N_2$ , which attributes to the unprecedented effect of  $CO_2$  calcination atmosphere on the photocatalytic  $H_2$  production activity from water.

Consequently, electron transport between heptazine rings and  $C_3N_4$  layers of  $C_3N_4$ -T- $CO_2$  proceeds more efficiently up to Pt nanoparticles than  $C_3N_4$ -T-air and  $C_3N_4$ -T- $N_2$ , resulting in the remarkably enhanced

Table 3

Transient absorption decay lifetimes ( $\tau_{abs}$ ) for  $C_3N_4$ -T-Y.

$C_3N_4$ -T-Y	$\tau_{abs1}$ (ps)	$\tau_{abs2}$ (ps)	$\tau_{abs,av}$ (ps)
$C_3N_4$ -T- $N_2$	36.0 (51%)	853 (49%)	436
$C_3N_4$ -T-air	31.0 (49%)	957 (51%)	503
$C_3N_4$ -T- $CO_2$	38.0 (45%)	1070 (55%)	605

$H_2$  production rate of  $C_3N_4$ -T- $CO_2$  photocatalyst.

#### 4. Conclusion

In summary,  $C_3N_4$ -T- $CO_2$  photocatalyst was developed for the first time through a one-step process by directly pyrolysis treatment of 3-amino-1,2,4-triazole in  $CO_2$  atmosphere with no additive.  $C_3N_4$ -T- $CO_2$  showed the higher  $H_2$  production ability under visible light irradiation than  $C_3N_4$ -T- $N_2$  and  $C_3N_4$ -T-air. The improvement of the photocatalytic activity for  $C_3N_4$ -T- $CO_2$  could be ascribed to the increased formation of  $NH_x$  sites to generate hydrogen-bonding interaction between  $C_3N_4$  layers and the inhibited degradation of heptazine rings to generate  $V_N$ .

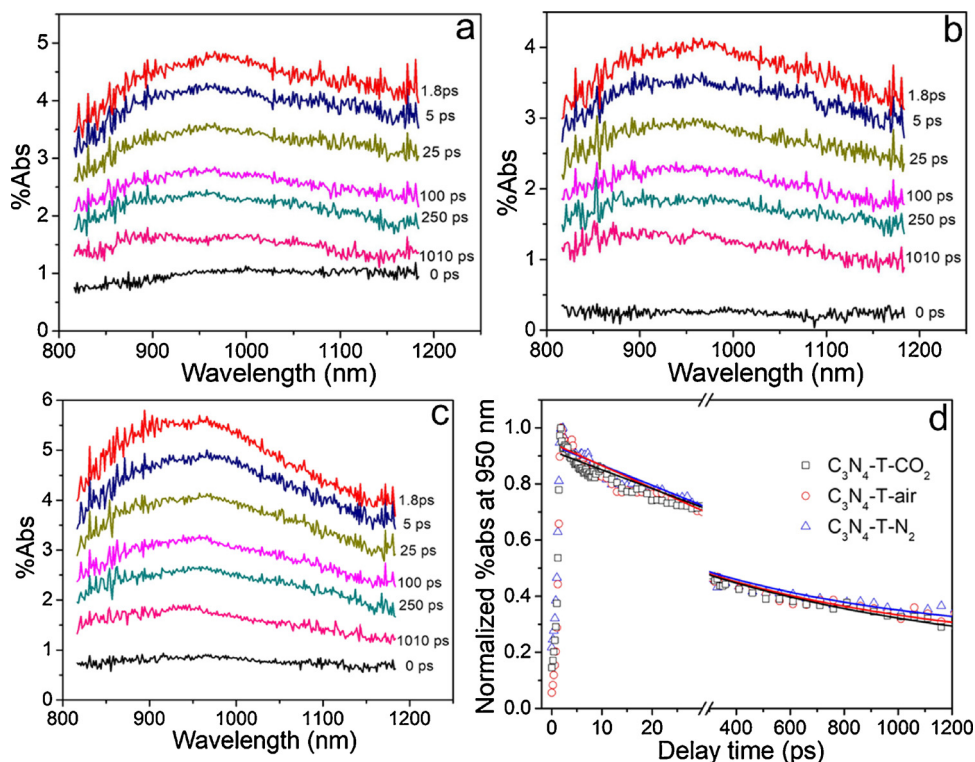
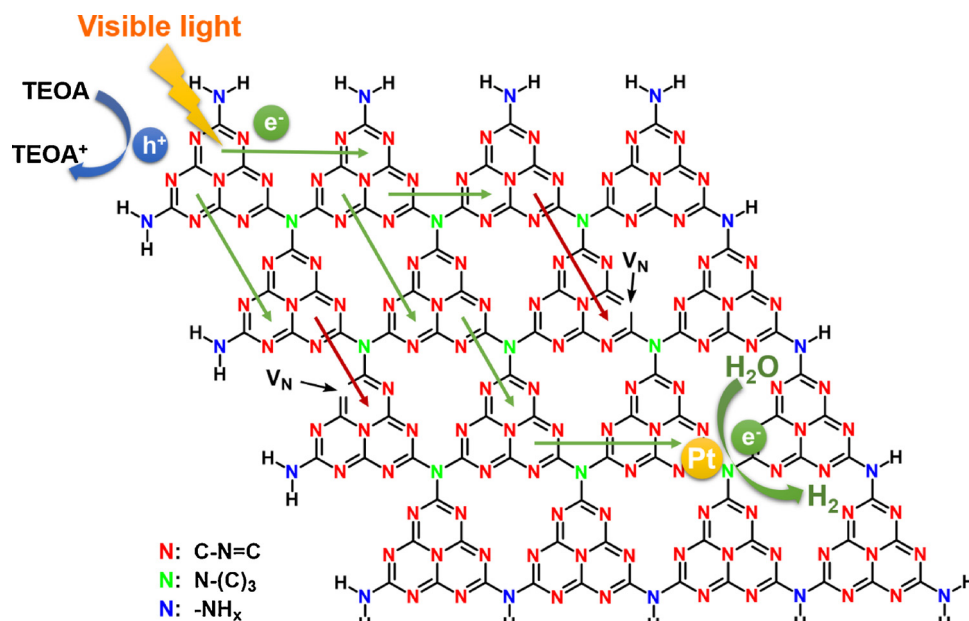


Fig. 7. Time-resolved diffuse reflectance spectra of  $C_3N_4$ -T- $N_2$  (a),  $C_3N_4$ -T-air (b), and  $C_3N_4$ -T- $CO_2$  (c), time profiles of normalized transient absorption at 950 nm for  $C_3N_4$ -T-Y after 420-nm laser pulse irradiation (d).



**Scheme 1.** C<sub>3</sub>N<sub>4</sub>-T-Y photocatalytic H<sub>2</sub> production mechanism involving band-gap excitation, charge separation to generate holes and electrons, holes removal by TEOA, electrons trapping by trap sites, electron transport processes between heptazine rings up to Pt nanoparticles, and proton reduction on the Pt nanoparticles.

with no charge transport ability under CO<sub>2</sub> calcination atmosphere. Charge transfer process of C<sub>3</sub>N<sub>4</sub>-T-CO<sub>2</sub> was systematically investigated by time-resolved fluorescence, single-particle fluorescence, and femto-second time-resolved transient absorption spectroscopies to reveal that the electron transport between heptazine rings and C<sub>3</sub>N<sub>4</sub> layers was effectively accelerated. Such unprecedented effect of CO<sub>2</sub> atmosphere was probably resulted from CO<sub>2</sub> ionic character for the interaction with the surface of g-C<sub>3</sub>N<sub>4</sub> during 3-amino-1,2,4-triazole calcination process. The present work puts forward a simple, facile, and economical method in designing highly effective g-C<sub>3</sub>N<sub>4</sub> photocatalyst for solar energy utilization.

## Acknowledgements

We are thankful for the help of the Comprehensive Analysis Center of SANKEN, Osaka University. This work has been partly supported by a Grant-in-Aid for Scientific Research (Project 25220806 and others) from the Ministry of Education, Culture, Sports, Science and Technology (MEXT) of Japanese Government. J.X. and Z.W. thank State Key Laboratory of Food Science and Technology, School of Food Science and Technology, International Joint Laboratory on Food Safety, and Collaborative Innovation Center of Food Safety and Quality Control in Jiangsu Province, Jiangnan University, National Natural Science Foundation of China (21707052), China Postdoctoral Science Foundation (2016M601718), Key Research and Development Program of Jiangsu Province (BE2017623), and Fundamental Research Funds for the Central Universities (JUSRP51714B).

## Appendix A. Supplementary data

Supplementary material related to this article can be found, in the online version, at doi:<https://doi.org/10.1016/j.apcatb.2018.09.023>.

## References

- [1] X. Wang, K. Maeda, A. Thomas, K. Takanabe, G. Xin, J.M. Carlsson, K. Domen, M. Antonietti, *Nat. Mater.* 8 (2009) 76–80.
- [2] D. Dontsova, S. Pronkin, M. Wehle, Z.P. Chen, C. Fetteckenhauer, G. Clavel, M. Antonietti, *Chem. Mater.* 27 (2015) 5170–5179.
- [3] W. Jiang, Q. Ruan, J. Xie, X. Chen, Y. Zhu, J. Tang, *Appl. Catal. B: Environ.* 236 (2018) 428–435.
- [4] Z.C. Sun, M.S. Zhu, M. Fujitsuka, A.J. Wang, C. Shi, T. Majima, *ACS Appl. Mater. Interfaces* 9 (2017) 30583–30590.
- [5] M. Zhang, W. Jiang, D. Liu, J. Wang, Y. Liu, Y. Zhu, *Appl. Catal. B: Environ.* 183 (2016) 263–268.
- [6] X. Bai, L. Wang, R. Zong, Y. Zhu, *J. Phys. Chem. C* 117 (2013) 9952–9961.
- [7] W.G. Tu, Y. Xu, J.J. Wang, B.W. Zhang, T.H. Zhou, S.M. Yin, S.Y. Wu, C.M. Li, Y.Z. Huang, Y. Zhou, Z.G. Zou, J. Robertson, M. Kraft, R. Xu, *ACS Sustain. Chem. Eng.* 5 (2017) 7260–7268.
- [8] S.W. Liu, F. Chen, S.T. Li, X.X. Peng, Y. Xiong, *Appl. Catal. B: Environ.* 211 (2017) 1–10.
- [9] J. Xu, Z.P. Wang, Y.F. Zhu, *ACS Appl. Mater. Interfaces* 9 (2017) 27727–27735.
- [10] J. Huang, W. Ho, X. Wang, *Chem. Commun.* 50 (2014) 4338–4340.
- [11] S.Z. Hu, X.Y. Qu, J. Bai, P. Li, Q. Li, F. Wang, L.J. Song, *ACS Sustain. Chem. Eng.* 5 (2017) 6863–6872.
- [12] G.H. Dong, W.K. Ho, C.Y. Wang, *J. Mater. Chem. A* 3 (2015) 23435–23441.
- [13] X.C. Wang, K. Maeda, X.F. Chen, K. Takanabe, K. Domen, Y.D. Hou, X.Z. Fu, M. Antonietti, *J. Am. Chem. Soc.* 131 (2009) 1680–1681.
- [14] J. Xu, L.W. Zhang, R. Shi, Y.F. Zhu, *J. Mater. Chem. A* 1 (2013) 14766–14772.
- [15] X. Bai, S. Yan, J. Wang, L. Wang, W. Jiang, S. Wu, C. Sun, Y. Zhu, *J. Mater. Chem. A* 2 (2014) 17521–17529.
- [16] S. Guo, Z. Deng, M. Li, B. Jiang, C. Tian, Q. Pan, H. Fu, *Angew. Chem. Int. Ed.* 55 (2016) 1830–1834.
- [17] M. Zhang, X. Bai, D. Liu, J. Wang, Y. Zhu, *Appl. Catal. B: Environ.* 164 (2015) 77–81.
- [18] M. Zhu, S. Kim, L. Mao, M. Fujitsuka, J. Zhang, X. Wang, T. Majima, *J. Am. Chem. Soc.* 139 (2017) 13234–13242.
- [19] X.W. Shi, M. Fujitsuka, S. Kim, T. Majima, *Small* 14 (2018) 1703277.
- [20] W.K. Ho, Z.Z. Zhang, W. Lin, S.P. Huang, X.W. Zhang, X.X. Wang, Y. Huang, *ACS Appl. Mater. Interfaces* 7 (2015) 5497–5505.
- [21] L. Luo, M. Zhang, P. Wang, Y.H. Wang, F. Wang, *New J. Chem.* 42 (2018) 1087–1091.
- [22] J. Oh, J.M. Lee, Y. Yoo, J. Kim, S.J. Hwang, S. Park, *Appl. Catal. B: Environ.* 218 (2017) 349–358.
- [23] J. Xu, Y. Wang, Y. Zhu, *Langmuir* 29 (2013) 10566–10572.
- [24] X.B. Li, G. Hartley, A.J. Ward, P.A. Young, A.F. Masters, T. Maschmeyer, *J. Phys. Chem. C* 119 (2015) 14938–14946.
- [25] Y.F. Li, R.X. Jin, Y. Xing, J.Q. Li, S.Y. Song, X.C. Liu, M. Li, R.C. Jin, *Adv. Energy Mater.* 6 (2016) 1601273.
- [26] Y.Y. Chai, Q.Q. Liu, L. Zhang, J. Ren, W.L. Dai, *Chin. J. Chem.* 35 (2017) 173–182.
- [27] Y.F. Li, M. Yang, Y. Xing, X.C. Liu, Y. Yang, X. Wang, S.Y. Song, *Small* 13 (2017) 1701552.
- [28] Q. Tay, P. Kanhere, C.F. Ng, S. Chen, S. Chakraborty, A.C.H. Huan, T.C. Sum, R. Ahuja, Z. Chen, *Chem. Mater.* 27 (2015) 4930–4933.
- [29] Q.H. Liang, Z. Li, Z.H. Huang, F.Y. Kang, Q.H. Yang, *Adv. Funct. Mater.* 25 (2015) 6885–6892.
- [30] X.P. Song, Q. Yang, X.H. Jiang, M.Y. Yin, L.M. Zhou, *Appl. Catal. B: Environ.* 217 (2017) 322–330.
- [31] D. Dontsova, C. Fetteckenhauer, V. Papaefthimiou, J. Schmid, M. Antonietti, *Chem. Mater.* 28 (2016) 772–778.
- [32] D.H. Park, K.S. Lakhi, K. Ramadass, M.K. Kim, S.N. Talapaneni, S. Joseph, U. Ravon,

- K. Al-Bahily, A. Vinu, *Chem. Eur. J.* 23 (2017) 10753–10757.
- [34] A. Savateev, S. Pronkin, J.D. Epping, M.G. Willinger, M. Antonietti, D. Dontsova, J. Mater. Chem. A 5 (2017) 8394–8401.
- [35] G.P. Mane, S.N. Talapaneni, K.S. Lakhi, H. Ilbeygi, U. Ravon, K. Al-Bahily, T. Mori, D.H. Park, A. Vinu, *Angew. Chem. Int. Ed.* 56 (2017) 8481–8485.
- [36] A.B. Jorge, D.J. Martin, M.T.S. Dhanoa, A.S. Rahman, N. Makwana, J.W. Tang, A. Sella, F. Cora, S. Firth, J.A. Darr, P.F. McMillan, *J. Phys. Chem. C* 117 (2013) 7178–7185.
- [37] A. Savateev, S. Pronkin, J.D. Epping, M.G. Willinger, C. Wolff, D. Neher, M. Antonietti, D. Dontsova, *ChemCatChem* 9 (2017) 167–174.
- [38] H.J. Yu, R. Shi, Y.X. Zhao, T. Bian, Y.F. Zhao, C. Zhou, G.I.N. Waterhouse, L.Z. Wu, C.H. Tung, T.R. Zhang, *Adv. Mater.* 29 (2017) 1605148.
- [39] P. Niu, M. Qiao, Y.F. Li, L. Huang, T.Y. Zhai, *Nano Energy* 44 (2018) 73–81.
- [40] J. Ding, W. Xu, H. Wan, D.S. Yuan, C. Chen, L. Wang, G.F. Guan, W.L. Dai, *Appl. Catal. B: Environ.* 221 (2018) 626–634.
- [41] M. Fujitsuka, A. Okada, S. Tojo, F. Takei, K. Onitsuka, S. Takahashi, T. Majima, *J. Phys. Chem. B* 108 (2004) 11935–11941.
- [42] R. Godin, Y. Wang, M.A. Zwiijnenburg, J.W. Tang, J.R. Durrant, *J. Am. Chem. Soc.* 139 (2017) 5216–5224.
- [43] O. Elbanna, P. Zhang, M. Fujitsuka, T. Majima, *Appl. Catal. B: Environ.* 192 (2016) 80–87.